

A similarity solution for two-phase fluid and heat flow near high-level nuclear waste packages emplaced in porous media

CHRISTINE DOUGHTY and KARSTEN PRUESS

Earth Sciences Division, Lawrence Berkeley Laboratory, 1 Cyclotron Road, Berkeley, CA 94720, U.S.A.

(Received 1 October 1988 and in final form 29 August 1989)

Abstract—The emplacement of a heat source, such as a high-level nuclear waste package, into a geologic medium causes strongly coupled thermal and hydrologic behavior. Under certain conditions, a heat pipe may develop, with significant impact on conditions at the heat source. In an infinite, homogeneous, permeable medium with a constant-strength linear heat source, the partial differential equations governing fluid and heat flows in a radial geometry can be converted to ordinary differential equations by using a similarity variable, $\eta = r/\sqrt{t}$. These equations are numerically integrated using an iterative 'shooting' method to provide a description of temperature, pressure, saturation, heat flow, gas flow, and liquid flow conditions around a heat source such as a nuclear waste package. The similarity solution is verified by numerical finite-difference simulations. Illustrative solutions are given for a range of hydrologic and thermal parameters, and the likelihood of heat-pipe development for conditions at several proposed repository sites is discussed.

1. INTRODUCTION

THE Yucca Mountain Project (YMP) is investigating the feasibility of constructing a geologic repository for high-level nuclear waste at Yucca Mountain, Nevada, in a partially saturated, highly fractured volcanic formation. Several recent mathematical modeling studies [1, 2] have examined the thermo-hydrologic behavior surrounding a repository in this geologic setting. Undisturbed conditions are such that temperature is well below the saturation temperature, so water is primarily in the liquid phase, and the initial heat transfer from a waste package is mainly conductive. As temperatures around the repository increase to the saturation temperature, evaporation increases and vapor partial pressure becomes appreciable. Heat-pipe effects may contribute to or even dominate heat transfer in this regime. With time the heat pipe moves away from the waste packages and leaves a gas-phase zone in which heat transfer is again conduction dominated. The conditions surrounding a waste package at some time after emplacement are shown schematically in Fig. 1.

In the heat-pipe region, heat transfer is primarily convective. Near the heat source, liquid water vaporizes, causing pressurization of the gas phase and gas-phase flow away from the heat source. The water vapor condenses in cooler regions away from the heat source and deposits its latent heat of vaporization there. This sets up a saturation profile, with liquid saturation increasing away from the heat source. The saturation gradient drives the backflow of the liquid phase toward the heat source through capillary forces. The liquid then vaporizes again and repeats the cycle. This convective heat transfer is very efficient com-

pared to conduction, so it is accompanied by very small temperature gradients.

The requirements for heat-pipe development are (1) the presence of a volatile fluid and (2) a mechanism by which gas-phase fluid can flow away from the heat source and liquid-phase fluid toward it. Gas-phase flow occurs if permeability of the medium is sufficiently high and the far-field pressure is lower than that at the heat source. Thus, heat-pipe behavior is unlikely in deep, water-saturated formations, where ambient pressure is much higher than open-hole or backfill pressure at the proposed repository. Liquid flow requires sufficient mobility and capillary pressure. Mobility depends on liquid saturation as well

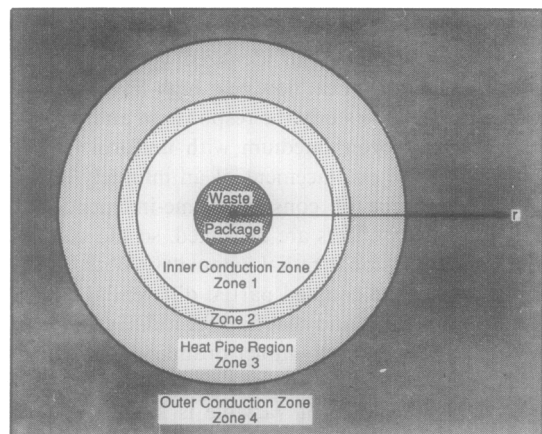


FIG. 1. Schematic of the conditions achieved at some time after waste emplacement (not to scale). Water is primarily in the liquid phase in zone 4, because $T < T_{sat}$; two-phase conditions prevail in zones 2 and 3, with $T \approx T_{sat}$; fluid in zone 1 is in the gas phase, with $T > T_{sat}$.

NOMENCLATURE

| | | | |
|------------------------|--|-----------------|--|
| C | volumetric heat capacity [J m ⁻³ K ⁻¹] | Greek symbols | |
| c_r | rock specific heat [J kg ⁻¹ K ⁻¹] | α_r | rock expansivity, $(1/\phi)\partial\phi/\partial T$ [K ⁻¹] |
| D_{va} | binary diffusion coefficient [m ² s ⁻¹] | β | ratio of kinematic viscosities for liquid- and gas-phase water |
| F | discrepancy vector at upper limit of integration | β_r | rock compressibility, $(1/\phi)\partial\phi/\partial P$ [Pa ⁻¹] |
| h | enthalpy [J kg ⁻¹] | γ | desired accuracy of endpoints of numerical integration |
| K | mobility ($K_j = kk_{rj}/\mu_j$, $j = 1, g$) [kg s ⁻¹ m ⁻¹ Pa ⁻¹] | δV_{Lj} | j th increment for Newton-Raphson iteration |
| k | intrinsic permeability [m ²] | ε | very small non-zero number |
| k_r | relative permeability | η | similarity variable, r/\sqrt{t} |
| M_c | energy accumulation term [J m ⁻³] | κ | thermal conductivity [W m ⁻¹ K ⁻¹] |
| M_w, M_a | mass accumulation terms [kg m ⁻³] | λ | parameter in the van Genuchten characteristic curves |
| P | pressure [Pa] | μ | dynamic viscosity [Pa s] |
| P_c | capillary pressure, $P_l - P_g$ [Pa] | ρ | density [kg m ⁻³] |
| Q_c | heat flow rate [W m ⁻¹] | σ | vapor-liquid interfacial tension [N m ⁻¹] |
| Q_w, Q_a | mass flow rates ($Q_m = Q_l^m + Q_g^m$, $m = w, a$) [kg s ⁻¹ m ⁻¹] | ϕ | porosity. |
| \bar{Q}_c | normalized heat flow rate, $Q_c/2\pi$ [W m ⁻¹] | | |
| \bar{Q}_w, \bar{Q}_a | normalized mass flow rates ($\bar{Q}_m = Q_m/2\pi$, $m = w, a$) [kg s ⁻¹ m ⁻¹] | Subscripts | |
| R | matrix of partial derivatives for Newton-Raphson iteration | a | air (also used as a superscript) |
| r | radial distance [m] | c | capillary, constant value |
| S | saturation | e | energy |
| T | temperature [°C] | g | gas phase |
| t | time [s] | L | lower limit of integration |
| u | internal energy [J kg ⁻¹] | l | liquid phase |
| V | vector of variables unspecified at lower limit of integration | r | rock, residual, relative |
| X | mass fraction | sat | at saturation (vapor-liquid equilibrium) |
| z | integration variable, $\ln(\eta)$. | U | upper limit of integration |
| | | w | water (also used as a superscript) |
| | | 0 | boundary condition, reference value. |

as the permeability of the medium, since liquid is immobile below a certain residual saturation.

This paper examines an idealized version of the problem of fluid and heat flow near high-level nuclear waste packages. We study the response of an infinite, homogeneous, porous medium with uniform initial conditions to the emplacement of an infinitely long, linear heat source of constant (time-independent) strength. Gravity effects are neglected, so the system has a one-dimensional radial symmetry. With these simplifications, the coupled partial differential equations governing fluid and heat flow for radial geometry can be transformed into simpler ordinary differential equations through the use of a similarity variable, $\eta = r/\sqrt{t}$. This change of variable is known as the Boltzmann transformation in heat conduction problems. It has been applied to the thermohydrologic behavior of geologic media by O'Sullivan [3], who used it to analyze geothermal well-test data. Other researchers [4, 5] have also used the similarity concept

for this purpose, but have limited themselves to simplified thermodynamic relationships to allow quasi-analytic solutions.

Following O'Sullivan [3], we consider the fully nonlinear problem with realistic thermodynamic relationships, which requires a numerical integration of the coupled differential equations. The main difference from O'Sullivan's treatment is that the mass flux boundary condition at $r = 0$, appropriate for geothermal production or injection wells, is here replaced by a heat flux boundary condition. Furthermore, we include capillary pressure and heat conduction effects. These are unimportant for the geothermal well-test problem but are essential for the heat-driven problem considered here. Our general mathematical treatment includes two fluid components, water and air, although the specific solutions presented here are for water only.

In the following sections, we first describe the development of the governing equations and the techniques

used for their integration. Next, we compare the similarity solution to results of numerical simulations, with excellent agreement. Finally, some characteristic features of thermohydrologic behavior in a geologic medium around a heat source are illustrated through application of the similarity solution.

2. BASIC EQUATIONS

The governing equations for fluid and heat flow for a single-component system in radial geometry as given by O'Sullivan [3] consist of a mass balance for water and an energy balance

$$\frac{\partial M_w}{\partial t} + \frac{1}{2\pi r} \frac{\partial Q_w}{\partial r} = 0 \tag{1}$$

$$\frac{\partial M_e}{\partial t} + \frac{1}{2\pi r} \frac{\partial Q_e}{\partial r} = 0. \tag{2}$$

If air is present in the system, a mass balance for air is also needed

$$\frac{\partial M_a}{\partial t} + \frac{1}{2\pi r} \frac{\partial Q_a}{\partial r} = 0. \tag{3}$$

The subscripts w, a, and e refer to water, air, and energy, respectively. To simplify the notation, we introduce normalized flux terms, given by $\tilde{Q} = Q/2\pi$. If the rock and fluid are assumed to be in local thermal equilibrium at all times, the accumulation terms are given by

$$M_m = \phi(S_l \rho_l X_l^m + S_g \rho_g X_g^m) \quad \text{for } m = w, a \tag{4}$$

$$M_e = (1 - \phi)\rho_r c_r T + \phi(S_l \rho_l \mu_l + S_g \rho_g \mu_g) \tag{5}$$

where ϕ is porosity, S is saturation, ρ is density, X is mass fraction, c is specific heat, T is temperature, and μ is internal energy. The subscripts l, g, and r refer to liquid phase, gas phase, and rock, respectively. Additionally, we have the conditions $S_l + S_g = 1$ and $X_l^m + X_g^m = 1$ for $m = w, a$. The assumption of local equilibrium between rock and fluid holds whenever the time required to reach local equilibrium, essentially the time it takes for diffusive heat flow to cross a rock grain, is much shorter than the times of interest in the problem. The thermohydrologic response shown in Fig. 1 propagates away from the heat source at a speed which is also controlled by diffusive heat flow, the dominant heat transfer mechanism in zone 4. However, the distances of interest are many orders of magnitude greater than rock grain dimensions, so the time scales are substantially longer than the time required to reach local equilibrium.

The mass flow rate for each component, the sum of liquid- and gas-phase flow rates, is given by Darcy's law, which is commonly used to describe both liquid- and gas-phase fluid flow in porous media. Darcy's law has been widely experimentally validated for porous-medium Reynolds numbers less than one [6]; by contrast, for the examples given in this paper the Reynolds numbers are less than 10^{-4} . When liquid-

and gas-phase fluids coexist in a porous medium, a relative permeability function may be used to account for the decrease in permeability of each phase due to interference from the other phase. In the gas phase there is also a flow component due to binary diffusion

$$\begin{aligned} \tilde{Q}_m = \tilde{Q}_l^m + \tilde{Q}_g^m = & \left(-\frac{kk_{r1}\rho_l X_l^m r}{\mu_l} \frac{\partial P_l}{\partial r} \right) \\ & + \left(-\frac{kk_{rg}\rho_g X_g^m r}{\mu_g} \frac{\partial P_g}{\partial r} - D_{va}\rho_g r \frac{\partial X_g^m}{\partial r} \right) \end{aligned} \tag{6}$$

for $m = w, a$

where k is intrinsic permeability, k_r is relative permeability, μ is dynamic viscosity, P is pressure, and D_{va} is the diffusion coefficient for vapor-air mixtures. Liquid and gas pressures are related by the capillary pressure through $P_l = P_g + P_c$. If no air is present, $X^w = 1$, $X^a = 0$, and the $m = a$ case of equations (4) and (6) is identically zero. The heat flow rate contains convective and conductive terms

$$\tilde{Q}_e = \sum_{\substack{j=w,a \\ m=w,a}} h_j^m \tilde{Q}_j^m - \kappa r \frac{\partial T}{\partial r} \tag{7}$$

where h is enthalpy and κ is thermal conductivity.

Equations (1)–(3), (6), and (7) make up a set of six coupled first-order partial differential equations for six unknowns (or primary variables). In single-phase regions S_g is constant, so \tilde{Q}_w , \tilde{Q}_a , \tilde{Q}_e , P_g , X_g^a , and T may be taken as the primary variables. In two-phase regions T depends on P_g and X through the saturation curve, so \tilde{Q}_w , \tilde{Q}_a , \tilde{Q}_e , P_g , X_g^a , and S_g become the primary variables. All other thermophysical properties can be expressed as functions of the primary variables, as described in the Appendix.

Note that by substituting equations (6) and (7) into equations (1)–(3) we could obtain a set of three second-order differential equations for three unknowns: P_g , X_g^a , and T in single-phase regions; and P_g , X_g^a , and S_g in two-phase regions. Although this set of equations may seem simpler than a set of six first-order equations, for numerical integration purposes it is preferable to treat first-order equations.

The uniform initial conditions are given by $\tilde{Q}_w = \tilde{Q}_a = \tilde{Q}_e = 0$, $P_g = P_0$, $X_g^a = X_0$, and $S_g = S_0$ for all r . The boundary conditions as $r \rightarrow 0$ are no mass flow ($\tilde{Q}_w = 0$, $\tilde{Q}_a = 0$) and constant heat flow ($\tilde{Q}_e = Q_{e0}/2\pi \equiv \tilde{Q}_{e0}$, where Q_{e0} is the heat source strength per unit length). The boundary conditions as $r \rightarrow \infty$ are unchanged from the initial values: $P_g = P_0$, $X_g^a = X_0$, and $S_g = S_0$.

Following O'Sullivan [3], we introduce a similarity variable $\eta = r/\sqrt{t}$ and rewrite the governing equations as

$$\begin{aligned} -\frac{\eta^2}{2} \frac{dM_m}{d\eta} + \frac{d\tilde{Q}_m}{d\eta} = 0 \quad \text{for } m = w, a \tag{8} \\ -\frac{\eta^2}{2} \frac{dM_e}{d\eta} + \frac{d\tilde{Q}_e}{d\eta} = 0 \tag{9} \end{aligned}$$

$$\tilde{Q}_m = \left(-K_l X_l^m \eta \frac{dP_l}{d\eta} \right) + \left(-K_g X_g^m \eta \frac{dP_g}{d\eta} - D_{va} \rho_g \eta \frac{dX_g^m}{d\eta} \right) \text{ for } m = w, a \quad (10)$$

$$\tilde{Q}_c = \sum_{j=1, g}^{m=w, a} h_j^m \tilde{Q}_j^m - \kappa \eta \frac{dT}{d\eta} \quad (11)$$

where liquid- and gas-phase mobilities have been defined as $K_l \equiv k k_{r,l} \rho_l / \mu_l$ and $K_g \equiv k k_{r,g} \rho_g / \mu_g$. Together, the initial and boundary conditions become boundary conditions given by

$$\tilde{Q}_w = 0, \tilde{Q}_a = 0, \tilde{Q}_c = \tilde{Q}_{c0} \text{ as } \eta \rightarrow 0 \quad (12)$$

$$P_g = P_0, X_g^a = X_0, S_g = S_0 \text{ as } \eta \rightarrow \infty. \quad (13)$$

It is well known that the 'natural' variable for axisymmetric heat-flow and fluid-flow problems is $\ln(r)$, rather than r itself. (The log term arises from the form of the Laplacian in radial coordinates.) In light of this fact, we make the substitution $z = \ln(\eta) = \ln(r/\sqrt{t})$. After replacing P_l with $P_g + P_c$ the governing equations become

$$-\frac{1}{2} \frac{dM_m}{dz} + e^{-2z} \frac{d\tilde{Q}_m}{dz} = 0 \text{ for } m = w, a \quad (14)$$

$$-\frac{1}{2} \frac{dM_c}{dz} + e^{-2z} \frac{d\tilde{Q}_c}{dz} = 0 \quad (15)$$

$$\tilde{Q}_m = -\left(K_l X_l^m + K_g X_g^m \right) \frac{dP_g}{dz} - K_l X_l^m \frac{dP_c}{dz} - D_{va} \rho_g \frac{dX_g^m}{dz} \text{ for } m = w, a \quad (16)$$

$$\tilde{Q}_c = - \sum_{m=w, a} \left[\left(h_l^m K_l X_l^m + h_g^m K_g X_g^m \right) \frac{dP_g}{dz} + h_l^m K_l X_l^m \frac{dP_c}{dz} + h_g^m D_{va} \rho_g \frac{dX_g^m}{dz} \right] - \kappa \frac{dT}{dz}. \quad (17)$$

The boundary conditions become

$$\tilde{Q}_w = 0, \tilde{Q}_a = 0, \tilde{Q}_c = \tilde{Q}_{c0} \text{ as } z \rightarrow -\infty \quad (18)$$

$$P_g = P_0, X_g^a = X_0, S_g = S_0 \text{ as } z \rightarrow \infty. \quad (19)$$

3. SOLUTION OF EQUATIONS

Equations (14)–(17) represent a set of six coupled first-order ordinary differential equations (ODEs). Solution of the system is straightforward in principle, by numerically integrating from $z = -\infty$ to ∞ , but in practice two complications arise that require special numerical techniques. One difficulty is posed by the 'mixed' boundary conditions, equations (18) and (19), which specify flux terms \tilde{Q}_w , \tilde{Q}_a , and \tilde{Q}_c at $z = -\infty$, while the thermodynamic functions P_g , X_g^a , and S_g satisfy boundary conditions at $z = \infty$. Thus, no complete set of starting values is available for integration, and an iterative approach known as the shooting

method [7] must be used (see below). Further difficulties arise from the non-linear dependence of the coefficients in equations (14)–(17) upon the thermodynamic parameters, especially in connection with multiphase flow effects (relative permeability, etc.) and phase change behavior.

We have achieved a computational solution for a simplified version of the problem stated by equations (14)–(17). The main simplification made is omission of the air component, which reduces the dimensionality of the problem from six coupled ODEs to a more easily tractable set of four ODEs. A further simplification is the restriction of admissible relative permeability functions to a mathematically well-behaved class of smooth functions. It is recognized that at the potential repository horizon at the Yucca Mountain site, significant flow effects will arise both from the presence of air [2] and from the extremely non-linear relative permeability relationships characteristic of a fractured-porous medium [8]. Our main objective in the present work has been to develop an implementation of the similarity solution technique under 'mixed' boundary conditions and to establish some reference cases for the behavior of strongly heat-driven flow systems with phase change. Work is underway to achieve a more realistic and detailed implementation of the specific conditions encountered at Yucca Mountain.

3.1. Shooting method

The first step of the shooting method [7] is to choose trial values for the unspecified variables at the lower limit of integration $z_L = -\infty$. From the general description of the thermohydrologic behavior of the system given in Section 1, we know that at $z_L = -\infty$ (long times; close to the heat source) gas-phase conditions prevail, so the unspecified variables are P_g and T , which can be defined to be the components of a vector V . The trial values at z_L are denoted V_L and T_L , or collectively, V_L . The numerical integration is then carried out from $z_L = -\infty$ to $z_U = \infty$. We use a fourth-order Runge–Kutta scheme, but other numerical integration algorithms could be used. The value of V at the upper limit of integration z_U is denoted V_U ; it can be viewed as a function of V_L . When air is not included in the analysis, liquid-phase conditions prevail at $z_U = \infty$ (initial time; far from the heat source), so the primary variables are P_l and T , and V_U has components P_U and T_U . Boundary conditions are specified at z_U for each component of V , so we can define a discrepancy vector F as the difference between V_U and the specified boundary conditions at z_U . The goal is to find an improved value of V_L , denoted V_L^* , that reduces the absolute value of F below an acceptable limit. We accomplish this via Newton–Raphson iteration; that is, we solve the following equation for V_L^* :

$$R(V_L^* - V_L) = -F \quad (20)$$

where \mathbf{R} is the Jacobian matrix, with components R_{ij} ($i, j = 1, 2$) given by

$$R_{ij} = \frac{\partial F_i}{\partial V_{Lj}} \quad (21)$$

The components of the matrix \mathbf{R} are obtained by numerical differentiation. This requires two additional numerical integrations, each using a modified value for one component of \mathbf{V}_L , denoted $V_{Lj} + \delta V_{Lj}$. The partial derivatives of equation (21) are then approximated by

$$\frac{\partial F_i}{\partial V_{Lj}} \approx \frac{F_i(V_{L1}, V_{Lj} + \delta V_{Lj}) - F_i(V_{L1}, V_{Lj})}{\delta V_{Lj}} \quad (22)$$

In general, because the equations are nonlinear, a numerical integration initialized with \mathbf{V}_L^* will not yield a zero value for \mathbf{F} , so the procedure must be repeated. Iteration continues until $|F_i| < \gamma|V_{Li}|$, and $|V_{Li}^* - V_{Li}| < \gamma|V_{Li}|$ for $i = 1, 2$, where γ represents the desired accuracy for \mathbf{V}_L and \mathbf{V}_U .

In a numerical procedure, using truly infinite integration limits is impossible; infinity must be approximated by suitably large finite values. As will be seen later, because of the nature of the present problem, the solution is insensitive to the values of the integration limits if they are beyond a certain range.

To use the shooting method, we need to express the governing equations in terms of derivatives of the primary variables with respect to the similarity variable. This is done through use of the chain rule for partial derivatives. Recall that different sets of primary variables are applicable for single- and two-phase conditions.

When air is not included in the analysis, the $m = a$ terms of equations (14)–(17) are not needed since X^a and \tilde{Q}_a are always zero, and the $m = w$ terms are greatly simplified since $X^w = 1$ throughout. In the following, the superscript w is omitted when no ambiguity results.

3.2. ODEs for single-phase regions

The distinction between P_g and P_l is not meaningful when only one phase exists, so the pressure is referred to simply as P in single-phase regions, and the chain rule takes the form

$$\frac{d}{dz} = \frac{dP}{dz} \frac{\partial}{\partial P} + \frac{dT}{dz} \frac{\partial}{\partial T} \quad (23)$$

and equations (14)–(17) become

$$-\frac{1}{2} \left(\frac{\partial M_w}{\partial P} \frac{dP}{dz} + \frac{\partial M_w}{\partial T} \frac{dT}{dz} \right) + e^{-2z} \frac{d\tilde{Q}_w}{dz} = 0 \quad (24)$$

$$-\frac{1}{2} \left(\frac{\partial M_c}{\partial P} \frac{dP}{dz} + \frac{\partial M_c}{\partial T} \frac{dT}{dz} \right) + e^{-2z} \frac{d\tilde{Q}_c}{dz} = 0 \quad (25)$$

$$\tilde{Q}_w = -K_j \frac{dP}{dz} \quad (26)$$

$$\tilde{Q}_c = -h_j K_j \frac{dP}{dz} - \kappa \frac{dT}{dz} \quad (27)$$

The subscript j is g for the gas phase and l for the liquid phase, which are labeled zones 1 and 4, respectively, in Fig. 1. Capillary pressure P_c is constant in single-phase regions, so $dP_c/dz = 0$. The accumulation terms simplify to

$$M_w = \phi \rho_j \quad (28)$$

$$M_c = (1 - \phi) \rho_c T + \phi \rho_j \mu_j \quad (29)$$

We would like to rearrange equations (24)–(27) to isolate the z -derivative terms on the left-hand side. Equation (26) can be trivially solved for dP/dz , which can be substituted into equation (27) to yield an expression for dT/dz . Equations (24) and (25) can be easily solved for $d\tilde{Q}_w/dz$ and $d\tilde{Q}_c/dz$, respectively, in terms of dP/dz and dT/dz . Altogether, we obtain the following set of equations to integrate for zones 1 and 4:

$$\frac{dP}{dz} = -\frac{\tilde{Q}_w}{K_j} \quad (30)$$

$$\frac{dT}{dz} = -\frac{\tilde{Q}_c - h_j \tilde{Q}_w}{\kappa} \quad (31)$$

$$\frac{d\tilde{Q}_w}{dz} = \frac{e^{2z}}{2} \left(\frac{\partial M_w}{\partial P} \frac{dP}{dz} + \frac{\partial M_w}{\partial T} \frac{dT}{dz} \right) \quad (32)$$

$$\frac{d\tilde{Q}_c}{dz} = \frac{e^{2z}}{2} \left(\frac{\partial M_c}{\partial P} \frac{dP}{dz} + \frac{\partial M_c}{\partial T} \frac{dT}{dz} \right) \quad (33)$$

3.3. ODEs for two-phase regions

For two-phase regions the chain rule takes the form

$$\frac{d}{dz} = \frac{dP_g}{dz} \frac{\partial}{\partial P_g} + \frac{dS_g}{dz} \frac{\partial}{\partial S_g} \quad (34)$$

and equations (14)–(17) become

$$-\frac{1}{2} \left(\frac{\partial M_w}{\partial P_g} \frac{dP_g}{dz} + \frac{\partial M_w}{\partial S_g} \frac{dS_g}{dz} \right) + e^{-2z} \frac{d\tilde{Q}_w}{dz} = 0 \quad (35)$$

$$-\frac{1}{2} \left(\frac{\partial M_c}{\partial P_g} \frac{dP_g}{dz} + \frac{\partial M_c}{\partial S_g} \frac{dS_g}{dz} \right) + e^{-2z} \frac{d\tilde{Q}_c}{dz} = 0 \quad (36)$$

$$\tilde{Q}_w = - \left[K_l \left(1 + \frac{\partial P_c}{\partial P_g} \right) + K_g \right] \frac{dP_g}{dz} - \left(K_l \frac{\partial P_c}{\partial S_g} \right) \frac{dS_g}{dz} \quad (37)$$

$$\tilde{Q}_c = - \left[h_l K_l \left(1 + \frac{\partial P_c}{\partial P_g} \right) + h_g K_g + \kappa \frac{dT}{dP_g} \right] \frac{dP_g}{dz} - \left(h_l K_l \frac{\partial P_c}{\partial S_g} \right) \frac{dS_g}{dz} \quad (38)$$

Because we have neglected vapor-pressure-lowering effects in the present work, there is no $\partial T/\partial S_g$ term in

equation (38), and the $\partial T/\partial P_g$ term is replaced by dT/dP_g . This reflects the simple dependence of temperature on pressure through the saturation curve. Note from equations (4) and (5) that the accumulation terms M_w and M_c contain terms ρ_l , ρ_g , u_l , u_g , and ϕ that depend on pressure both explicitly, and implicitly through temperature, since $T = T_{sat}(P_g)$.

As in the single-phase region, we would like to rearrange equations (35)–(38) to explicitly obtain dP_g/dz and dS_g/dz from equations (37) and (38), so that the remaining unknowns $d\tilde{Q}_w/dz$ and $d\tilde{Q}_c/dz$ can be found by simple substitution into equations (35) and (36). To accomplish this, it is necessary to divide by K_l , which is proportional to the liquid relative permeability k_{rl} . By definition, $k_{rl} > 0$ when $S_l > S_{lr}$, where S_{lr} is the residual liquid saturation. In the present work, to avoid the complications arising from $K_l = 0$ for $S_l \leq S_{lr}$, we consider only cases where $S_{lr} = 0$, so $k_{rl} > 0$ throughout the two-phase zone, and there is never a problem dividing by K_l . A two-phase region with a mobile liquid phase is shown as zone 3 in Fig. 1. In future work we plan to address the situation where $S_{lr} > 0$ and a two-phase zone with an immobile liquid phase develops (zone 2 in Fig. 1).

With the condition $K_l > 0$, equations (37) and (38) can be solved for dP_g/dz and dS_g/dz . Equations (35) and (36) can be solved for $d\tilde{Q}_w/dz$ and $d\tilde{Q}_c/dz$, respectively, in terms of dP_g/dz and dS_g/dz . Altogether, we obtain the following set of equations to integrate for zone 3:

$$\frac{dP_g}{dz} = - \frac{\tilde{Q}_c - h_l \tilde{Q}_w}{(h_g - h_l)K_g + \kappa \frac{dT}{dP_g}} \quad (39)$$

$$\frac{dS_g}{dz} = \left\{ \tilde{Q}_c \left[K_l \left(1 + \frac{\partial P_c}{\partial P_g} \right) + K_g \right] - \tilde{Q}_w \left[h_l K_l \left(1 + \frac{\partial P_c}{\partial P_g} \right) + h_g K_g + \kappa \frac{dT}{dP_g} \right] \right\} / \left\{ (h_g - h_l)K_g + \kappa \frac{dT}{dP_g} \right\} K_l \frac{\partial P_c}{\partial S_g} \quad (40)$$

$$\frac{d\tilde{Q}_w}{dz} = \frac{e^{2z}}{2} \left(\frac{\partial M_w}{\partial P_g} \frac{dP_g}{dz} + \frac{\partial M_w}{\partial S_g} \frac{dS_g}{dz} \right) \quad (41)$$

$$\frac{d\tilde{Q}_c}{dz} = \frac{e^{2z}}{2} \left(\frac{\partial M_c}{\partial P_g} \frac{dP_g}{dz} + \frac{\partial M_c}{\partial S_g} \frac{dS_g}{dz} \right) \quad (42)$$

3.4. Transitions between zones

In order to make the transition in primary variables required at phase changes, at each step in the numerical integration the current phase conditions are checked. For the gas phase (zone 1), as equations (30)–(33) are being integrated, the temperature T is compared to the saturation temperature for the pressure, $T_{sat}(P)$. If $T > T_{sat} + \varepsilon$, where $\varepsilon \approx 10^{-8}$, the gas-phase/two-phase transition has not been reached yet. The integration step is accepted, and the integration

proceeds, still in zone 1. If $T < T_{sat} - \varepsilon$, the integration has gone beyond the phase-change point. The step is then rejected and attempted again using a smaller step size. If $T_{sat} - \varepsilon < T < T_{sat} + \varepsilon$, the phase-change point has been reached, and the transition to two-phase conditions (zone 3) is made, with gas-phase saturation S_g replacing T as the primary variable and equations (39)–(42) replacing equations (30)–(33) in the integration. At the zone 1/zone 3 transition, S_g is initialized as $1 - S_l^{\min}$, where S_l^{\min} is the minimum liquid saturation for which liquid relative permeability $k_{rl} > \varepsilon$. The value of S_l^{\min} depends on the form of the relative permeability function.

At each step in zone 3, as equations (39)–(42) are being integrated, T is set to $T_{sat}(P_g)$ and S_g is compared to zero. If $S_g > \varepsilon$, the two-phase/liquid transition has not been reached yet; the step is accepted, and the integration proceeds, still in zone 3. If $S_g < -\varepsilon$, the phase-change point has been passed. The step is then rejected and repeated using a smaller step size. If $-\varepsilon < S_g < \varepsilon$, the phase-change point has been reached, and the transition to zone 4 is made, with T becoming the primary variable and equations (30)–(33) replacing equations (39)–(42) in the integration.

The parameter ε is chosen to be very small compared to the numbers it is added to or multiplied by, but large enough to be treated accurately by a finite-precision computer. We take $\varepsilon = 10^{-n}$, where n is half the number of significant figures the computer uses to express real numbers. The present work was carried out on a Cray X-MP at the National Magnetic Fusion Energy Computer Center, Lawrence Livermore National Laboratory. This computer expresses real numbers with approximately 16 significant figures, so $\varepsilon = 10^{-8}$.

3.5. Step-size control

At each step in the numerical integration, the results are compared with results obtained by splitting the step into two half-steps. If the results agree within a specified criterion, the step is accepted and step size is increased for the next step; if they do not, the step is rejected and repeated using a smaller step size.

4. COMPUTATIONAL PROCEDURE

As an example of the application of the similarity solution, we consider a heat source of strength $Q_{e0} = 200 \text{ W m}^{-1}$ emplaced in a porous medium that has the material properties and characteristic curves given in Table 1. The initial conditions are $P_0 = 0.1013 \text{ MPa}$ and $T_0 = 26^\circ\text{C}$. For the most part, the properties and functions described in Table 1 are representative of a laboratory sand pack used to study steady-state heat-pipe behavior [9]. The intrinsic permeability k has been decreased by a factor of 10 and the rock compressibility $\beta_r = (1/\phi)\partial\phi/\partial P$ increased by a factor of 10 to simplify the computation. Neither change is necessary for the method to

Table 1. Material properties, characteristic curves, and boundary conditions used for the similarity-solution results shown in Figs. 3 and 4

| Material properties | | |
|---------------------------------|------------|--|
| intrinsic permeability | k | 10^{-13} m^2 |
| initial porosity | ϕ_0 | 0.40 |
| rock compressibility | β_r | 10^{-7} Pa^{-1} |
| rock expansivity | α_r | 0 K^{-1} |
| rock density | ρ_r | 2580 kg m^{-3} |
| rock specific heat | c_r | $840 \text{ J kg}^{-1} \text{ K}^{-1}$ |
| thermal conductivity [10, 11]: | | |
| liquid-saturated rock | κ_l | $1.13 \text{ W m}^{-1} \text{ K}^{-1}$ |
| gas-saturated rock | κ_g | $0.582 \text{ W m}^{-1} \text{ K}^{-1}$ |
| Characteristic curves | | |
| relative permeability [12, 13]: | | |
| liquid | k_{rl} | S_l^3 |
| vapor | k_{rg} | S_g^3 |
| capillary pressure [14] | P_c | $-\sigma(T)(\phi/k)^{1/2}f$ $f = 1.417S_g - 2.12S_g^2 + 1.263S_g^3$ |
| Boundary conditions | | |
| $z \rightarrow -\infty$ | Q_{w0} | 0 |
| | Q_{e0} | 200 W m^{-1} |
| $z \rightarrow \infty$ | P_0 | 101325 Pa |
| | T_0 | 26°C |

work in general; the effects of the changes are described in Section 6.

The first step in applying the similarity solution is to choose z_L and z_U , the limits of integration, and trial values for T and P at z_L , which are denoted $T(z_L) = T_L$ and $P(z_L) = P_L$. Some clues are provided by examining the much simpler problem of a heat source emplaced in a medium in which all heat transfer is conductive. For constant thermal conductivity κ_c and heat capacity C_c , this problem has an analytical solution given in terms of the exponential integral [15]

$$Q_c = \frac{Q_{e0}}{2\pi} \exp\left(\frac{-C_c \eta^2}{4\kappa_c}\right) \quad (43)$$

$$T = T_0 + \frac{Q_{e0}}{2\pi\kappa_c} \int_{\eta}^{\infty} \frac{1}{\eta'} \exp\left(\frac{-C_c \eta'^2}{4\kappa_c}\right) d\eta'$$

$$= T_0 - \frac{Q_{e0}}{4\pi\kappa_c} \text{EI}\left(\frac{-C_c \eta^2}{4\kappa_c}\right). \quad (44)$$

Figure 2 shows the temperature and heat-flow profiles for thermal properties corresponding to liquid water ($\kappa_c = 1.13 \text{ W m}^{-1} \text{ K}^{-1}$, $C_c = 2.9 \text{ MJ m}^{-3} \text{ K}^{-1}$) and water vapor ($\kappa_c = 0.582 \text{ W m}^{-1} \text{ K}^{-1}$, $C_c = 1.3 \text{ MJ m}^{-3} \text{ K}^{-1}$) saturating a medium that has the thermal properties given in Table 1. Appropriate limits of integration for this problem would be $z_L < -10$ and $z_U > -5$, beyond the region of changing heat flow. Anticipating variations in fluid flow as well as heat flow, we arbitrarily extend the limits in both directions to obtain $z_L = -15$ and $z_U = -3$ as tentative limits for the similarity-solution integration. For a vanishingly short heat pipe, that is, a direct transition from gas to liquid phase, T_L would fall between the

$T(z_L)$ values for the liquid and gas curves shown in Fig. 2, which are 252 and 468°C. Thus, we take $T_L = (252 + 468)/2 = 360^\circ\text{C}$ as an initial guess for the temperature boundary condition. If the length of the heat-pipe region turns out to be substantial, this value of T_L will be too high. The conduction solution does not provide any information on pressure so we take $P_L = P_0 = 0.1013 \text{ MPa}$.

The numerical integration from $z_L = -15$ to $z_U = -3$ results in $T_U = 45.6^\circ\text{C}$ and $P_U = 0.0509 \text{ MPa}$ (Table 2). For this 'first shot', T_U and P_U are not very close to T_0 and P_0 , which is not a surprising result in

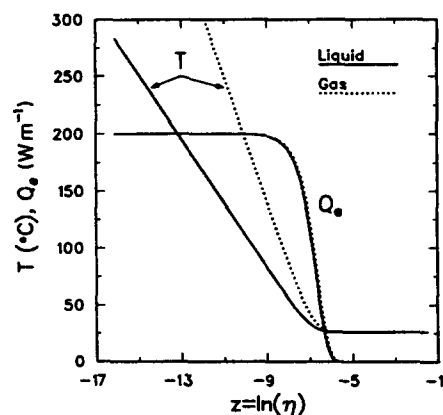


FIG. 2. Conduction-only temperature and heat-flow profiles for liquid-saturated and gas-saturated media. For this and all successive figures, $z = \ln(\eta) = \ln(r/\sqrt{t})$, with r in meters and t in seconds.

Table 2. Details of the shooting method for the results shown in Fig. 3

| Shot | Increment | P_L (MPa) | T_L (°C) | P_U (MPa) | T_U (°C) |
|-----------|--------------|-------------|------------|-------------|------------|
| 1 | — | 0.10133 | 360.00 | 0.05088 | 45.62 |
| | δP_L | 0.10033 | 360.00 | 0.04982 | 45.23 |
| | δT_L | 0.10133 | 354.00 | 0.05090 | 42.76 |
| 2 | — | 0.14864 | 279.86 | 0.10064 | 22.11 |
| | δP_L | 0.14764 | 279.86 | 0.09960 | 21.82 |
| | δT_L | 0.14864 | 273.86 | 0.10065 | 19.07 |
| 3 | — | 0.14929 | 287.19 | 0.10133 | 25.99 |
| Converged | | | | | |

Increments: $\delta P_L = -0.001$ MPa, $\delta T_L = -6.0^\circ\text{C}$ (comparable results are obtained for increment values in the range $10^{-6} < |\delta P_L| < 0.02$ and $0.006 < |\delta T_L| < 24$).

Accuracy: $\gamma = 0.03$.

view of the simplistic initial guesses used. The Newton–Raphson iteration requires that the integration be repeated twice for each shot, using a modified value of P_L , $P_L + \delta P_L$, in one case and a modified value of T_L , $T_L + \delta T_L$, in the other. The values chosen for δP_L and δT_L must be small enough to yield an accurate approximation for the partial derivatives given in equation (22) but large compared to the errors generated in the numerical integration. By solving equation (20) we obtain improved values of P_L and T_L for the second shot. After three shots the solution converges, as shown in Table 2. Figure 3 shows the temperature and pressure profiles for each shot. In all figures, pressure shown in the two-phase region is P_g . Each integration takes about 420 steps; the whole procedure uses 20 s of CPU time on a Cray X-MP computer.

Sometimes an initial guess may be too poor to allow the numerical integration to be completed. For example, if T_L is too small, temperatures drop below 0°C and the equations of state for liquid water and vapor are not applicable. Without values of T_U and P_U , the Newton–Raphson iteration cannot be done. Other times the integration can be completed, but

the T_U and P_U values are so far from T_0 and P_0 that the Newton–Raphson iteration diverges. In practice, the usual procedure is to perform a numerical integration with an initial guess for T_L and P_L , plot the resulting T and P profiles, and choose improved values of T_L and P_L based on general features of the profiles. After one or two repetitions of this procedure, the profiles should be close enough to the true solution to allow efficient use of Newton–Raphson iteration.

Figure 4(a) shows the pressure, temperature, and saturation profiles for the converged solution, while the solid lines in Fig. 4(b) show the liquid, gas, water (liquid plus gas), and heat flows. The lower limit of integration z_L is beyond the region where fluid or heat flow vary, but at $z_U = -3$, Q_1 is still changing, so the integration should be continued. Both T and P are nearly constant around $z = -3$, so extending the integration will not require additional Newton–Raphson iterations. The dashed lines show Q_l , Q_g , and Q_e values obtained by continuing the integration from $z_L = -3$ to $z_U = -1.4$. This part of the integration requires 6780 steps, significantly more than the 420 required to integrate between $z_L = -15$ and $z_U = -3$. The form of equations (32) and (33) dictates that as z increases, step size decreases. This decrease becomes significant for $z > -5$, and overwhelming for $z > -1$.

Note from the definition of the similarity variable that Fig. 4 represents both a spatial distribution at a given time, with distance from the heat source increasing from left to right, and a time sequence at a given point in space, with time increasing from right to left. The signature of the heat pipe is the large liquid–vapor counterflow shown in Fig. 4(b), with net water flow nearly zero, and the corresponding nearly isothermal zone shown in Fig. 4(a). The larger temperature gradient and constant pressure within the vapor zone ($z > -11.8$) indicate that conduction is the dominant heat-transfer mechanism there. In the liquid zone ($z > -9.6$) there are two domains. Just beyond the two-phase zone there is a region with a linear temperature gradient, constant heat flow, and small mass flow, which indicates a conductive regime. At the location of the heat-flow front ($z \approx -7$), mass flow

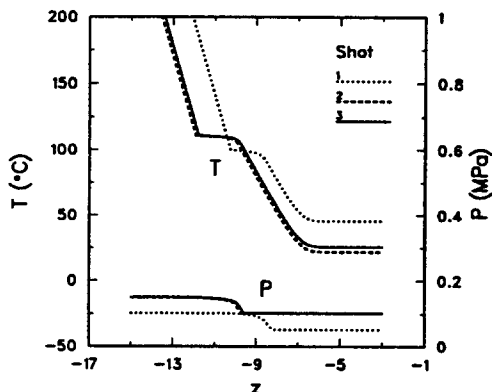


FIG. 3. Temperature and pressure profiles illustrating the shooting method.

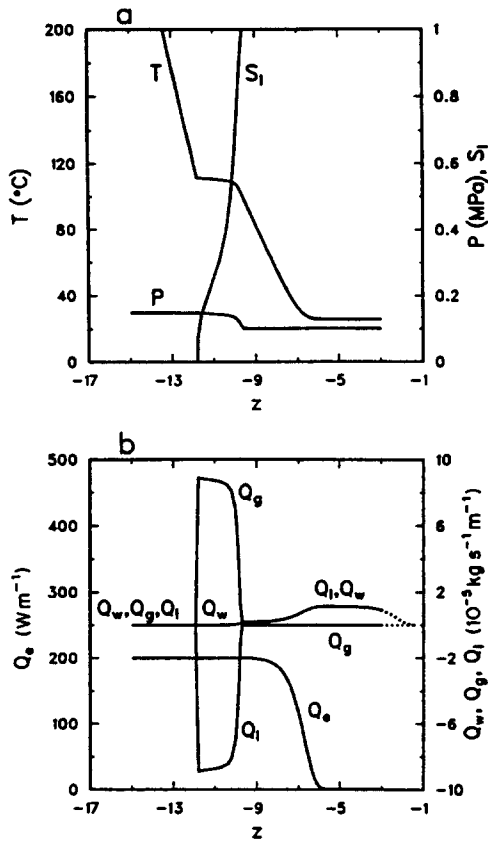


FIG. 4. Temperature, pressure, and saturation profiles (a) and heat-, mass-, liquid-, and gas-flow profiles (b) for the problem described in Table 1.

away from the heat source increases. This out flow is necessary because the water vapor forming at the heat pipe is much less dense than the liquid water it replaces. The out flow occurs at the heat-flow front because the changing heat-flow rate causes differential heating of the liquid; liquid density differences then create the small pressure gradients that drive the out flow.

5. COMPARISON WITH NUMERICAL SIMULATIONS

The numerical model TOUGH [16] has been used to verify the similarity solution. TOUGH (transport of unsaturated groundwater and heat) calculates the two-phase flow of air and water in gaseous and liquid phases together with heat flow using the governing equations shown in Section 2. As described in the Appendix, material properties vary with pressure, temperature, and saturation. TOUGH uses an integral-finite-difference method that is applicable for one-, two-, or three-dimensional flow problems in porous or fractured porous media. The governing mass- and energy-balance equations are strongly non-

linear and are solved simultaneously, using Newton-Raphson iteration.

A one-dimensional, radial, calculational mesh with 90 elements is used to calculate pressure, temperature, and saturation in a porous medium surrounding a heat source of strength $Q_{e0} = 200 W m^{-1}$. Material properties and mesh dimensions are given in Table 3. Initial conditions everywhere are $P = 0.1013 MPa$, $T = 26^\circ C$, and $S_1 = 1$. The innermost element of the mesh includes the heat source; at the outermost element P and T are held constant. This approximate implementation of the similarity-solution boundary conditions for $z = -\infty$ and ∞ is unavoidable with a numerical model, which is necessarily of finite extent.

A simulation for 10 000 years takes 475 time steps and requires 8.6 min of CPU time on a Cray X-MP. Figure 5, which shows temperature, pressure, and saturation (Fig. 5(a)) and heat, mass, liquid, and gas flows (Fig. 5(b)) vs radial distance for a series of times, illustrates the development of the heat pipe and its migration away from the heat source. Figure 6 shows the same variables plotted as a function of $z = \ln(r/\sqrt{t})$, with profiles for 21 different times displayed. The close agreement between the profiles for different times verifies the use of the similarity concept for this problem. The small spread between the profiles can be understood from the observation by Schroeder *et al.* [17] that, for a numerical solution calculated on a finite-difference grid, there is only an approximate invariance with respect to the similarity variable, because of the finite grid spacing. Data from the innermost and outermost mesh elements are not included in Fig. 6 because grid effects are most pronounced where boundary conditions are implemented. The greater spread between the profiles at the inner limit of the heat pipe results from early-time profiles, when the heat source is close to the heat pipe. Later-time profiles, when the heat pipe has moved further from the heat source, are more accurate. At still later times, the liquid flow away from the heat source reaches the constant-pressure boundary at the outer limit of the mesh, so the mesh no longer represents an infinite medium properly, which causes the liquid flow profiles to diverge. Figure 7 compares an intermediate-time profile, for which mesh effects are minimal, and the similarity solution. The match is excellent.

6. ILLUSTRATIVE EXAMPLES

In this section we examine significant features of the response of a porous medium to emplacement of a strong heat source in one-dimensional radial geometry. In particular, the dependence of system behavior upon major thermal and hydrologic parameters is illustrated by way of calculated examples.

6.1. Relative permeability functions

Five different relative permeability functions are described in Table 4 and plotted in Fig. 8(a) as a

Table 3. Material properties, characteristic curves, and mesh spacing used for the TOUGH simulation

| Material properties | | |
|--------------------------------|--------------------------------|---|
| intrinsic permeability | k | 10^{-15} m^2 |
| initial porosity | ϕ_0 | 0.40 |
| rock compressibility | β_r | 10^{-8} Pa^{-1} |
| rock expansivity | α_r | 0 K^{-1} |
| rock density | ρ_r | 2600 kg m^{-3} |
| rock specific heat | c_r | $700 \text{ J kg}^{-1} \text{ K}^{-1}$ |
| thermal conductivity [10, 11]: | | |
| liquid-saturated rock | κ_l | $1.13 \text{ W m}^{-1} \text{ K}^{-1}$ |
| gas-saturated rock | κ_g | $0.582 \text{ W m}^{-1} \text{ K}^{-1}$ |
| Characteristic curves | | |
| relative permeability : | | |
| liquid | k_{rl} | S_l |
| vapor | k_{rg} | S_g |
| capillary pressure [14] | P_c | $-\sigma(T)(\phi/k)^{1/2}f$ $f = 1.417S_g - 2.12S_g^2 + 1.263S_g^3$ |
| Mesh spacing | | |
| Element | Size | Comments |
| 1 | $\Delta r_1 = 0.016 \text{ m}$ | Contains 200 W m^{-1} heat source. |
| 2 | $\Delta r_2 = 0.010 \text{ m}$ | |
| $i, i = 3, 90$ | $\Delta r_i = a\Delta r_{i-1}$ | $a = 1.138$ Center of element 90 is 6755 m; P_g and T are held fixed there. |

function of liquid saturation S_l . The linear, cubic [12, 13], and Corey [18] functions are commonly encountered in the petroleum literature; the Verma *et al.* [19] function was developed from laboratory experiments on liquid-vapor water flow; and the van Genuchten [20] liquid relative permeability function comes from the soil sciences. As is traditional in the soil-science approach to fluid flow, no gas-phase relative permeability function is presented in the van Genuchten work [20], so we take $k_{rg} = 1 - k_{rl}$. For the parameter λ we use 0.45 [21]. Figure 8(b) shows the temperature, pressure, and saturation profiles calculated with the different relative permeability functions and the other values from Table 1. There is a large variation in heat-pipe length. The cubic and Corey curves (Fig. 8(a)) are quite similar and yield similar profiles (Fig. 8(b)) with relatively short heat pipes. The linear and Verma curves (Fig. 8(a)) are similar for k_{rg} but quite different for k_{rl} . The corresponding saturation profiles (Fig. 8(b)) are similar for large values of S_l but very different for $S_l < 0.25$, which results in heat pipes of very different length. The van Genuchten k_{rg} curve is quite different from all the others, and the resulting saturation profile is also distinct, but the heat-pipe length is similar to that for the linear curves. Note that the linear and van Genuchten curves share the property that $k_{rl} + k_{rg} = 1$ (for the other cases $k_{rl} + k_{rg} < 1$) and that the heat-pipe length is significantly greater for these cases.

The effect of the relative permeability function can be predicted qualitatively by examining equation (40)

for dS_g/dz . To facilitate comparison with the figures, which show S_l rather than S_g , we replace dS_g/dz with $-dS_l/dz$

$$\frac{dS_l}{dz} = - \left\{ \bar{Q}_c \left[K_l \left(1 + \frac{\partial P_c}{\partial P_g} \right) + K_g \right] - \bar{Q}_w \left[h_l K_l \left(1 + \frac{\partial P_c}{\partial P_g} \right) + h_g K_g + \kappa \frac{dT}{dP_g} \right] \right\} / \left\{ (h_g - h_l) K_g + \kappa \frac{dT}{dP_g} \right\} K_l \frac{\partial P_c}{\partial S_g} \quad (45)$$

When heat-pipe effects are significant, as in the examples shown in Figs. 4(a), (b) and 8(b), equation (45) can be simplified. Figure 4(b) shows that in the two-phase region net water flow \bar{Q}_w is zero and heat flow \bar{Q}_c is constant. Furthermore, $\partial P_c / \partial P_g$ is generally small, and $\kappa dT/dP_g$ is small compared to $(h_g - h_l) K_g$ if conduction is small compared to convection, that is, if the heat-pipe region is nearly isothermal. Thus, an approximate version of equation (45) may be written

$$\frac{dS_l}{dz} \approx - \frac{\bar{Q}_c}{(h_g - h_l) \frac{\partial P_c}{\partial S_g}} \left(\frac{K_l + K_g}{K_g K_l} \right) = - \frac{\bar{Q}_c}{(h_g - h_l) \frac{\partial P_c}{\partial S_g}} \left(\frac{1}{K_g} + \frac{1}{K_l} \right) \quad (46)$$

where $K_g = k k_{rg} \rho_g / \mu_g$ and $K_l = k k_{rl} \rho_l / \mu_l$. Under the

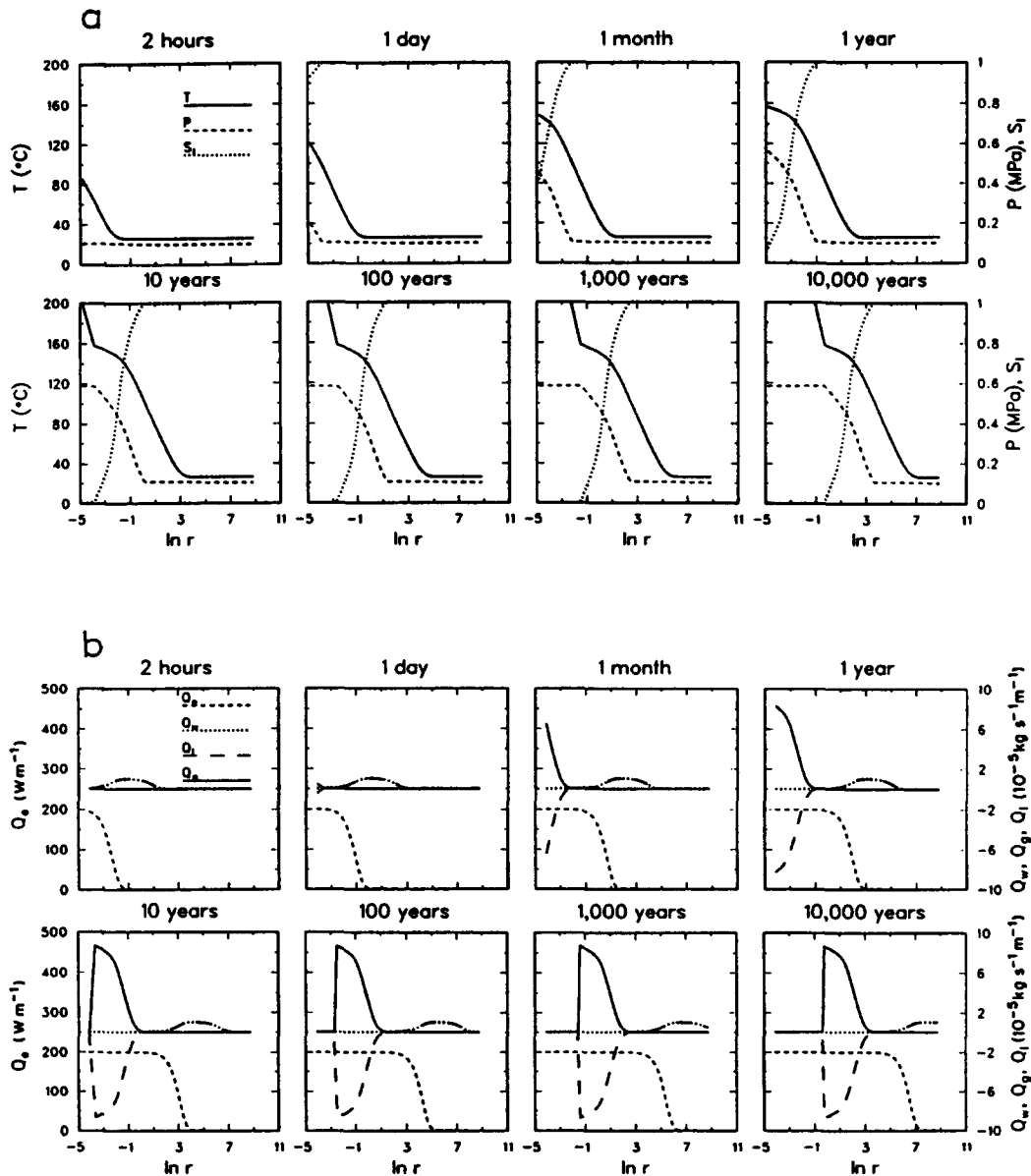


FIG. 5. TOUGH simulation for temperature, pressure, and saturation (a) and heat, mass, liquid, and gas flows (b) as a function of radial distance (in meters) for a series of times.

nearly constant-temperature and constant-pressure conditions of the heat-pipe region, ρ_g , ρ_l , μ_g , and μ_l are approximately constant and can be combined into a parameter β , defined as the ratio of the kinematic viscosities of the liquid and gas

$$\beta = \frac{\mu_l/\rho_l}{\mu_g/\rho_g} \quad (47)$$

For $P_g \approx 0.1$ MPa and $T \approx 100^\circ\text{C}$, $\beta \approx 0.01$. Equation (46) may then be written as

$$\frac{dS_l}{dz} \approx -\frac{\bar{Q}_e}{(h_g - h_l) \frac{\partial P_c}{\partial S_g} k \rho_g} \left(\frac{1}{k_{rg}} + \beta \right) \quad (48)$$

Thus, dS_l/dz is controlled by the smaller of k_{rg} and k_{rl}/β . For large values of S_l , k_{rg} is the controlling factor. Figure 8(a) shows that the value of k_{rg} for the van Genuchten function is far larger than the rest, while the cubic and Corey functions are similar and very small, and the linear and Verma functions are similar and of intermediate magnitude. This variation is reflected in the upper portion of the saturation profiles in Fig. 8(b), where the van Genuchten S_l profile has the smallest slope, the cubic and Corey profiles are steepest, and the linear and Verma profiles are in between. For small values of S_l , k_{rl} is the controlling factor. Figure 8(a) shows that the values of k_{rl} for the linear and Verma functions are very different, leading

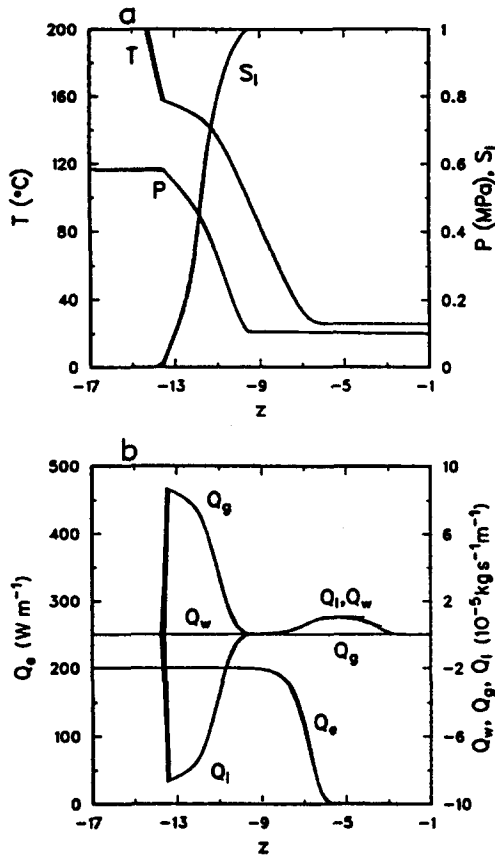


FIG. 6. TOUGH simulation for temperature, pressure, and saturation (a) and heat, mass, liquid, and gas flows (b) as a function of $z = \ln(r/\sqrt{t})$, with profiles from 21 different times included.

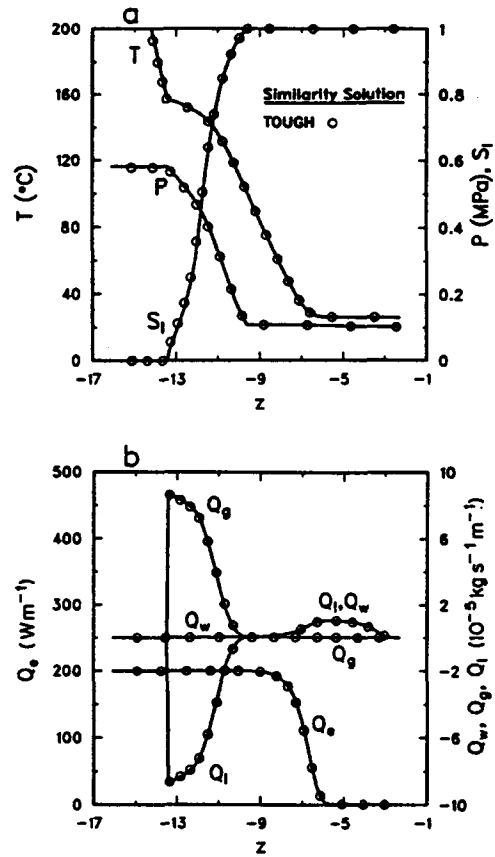


FIG. 7. A comparison between the 200-year TOUGH result and the similarity solution for temperature, pressure, and saturation profiles (a) and heat-, mass-, liquid-, and gas-flow profiles (b).

to the diverging saturation profiles seen in Fig. 8(b). The k_{ri} curves for the cubic and Corey functions are similar, so the saturation profiles remain close together. The Verma and cubic functions use the same k_{ri} curve, as evidenced by the parallel saturation profiles for small values of S_l . All the k_{ri} curves except the linear one become vanishingly small as S_l approaches zero, which leads to the sharp down turn in the saturation profile that is characteristic of all cases except the linear one.

6.2. Intrinsic permeability

Figure 9 shows the temperature, pressure, and saturation (Fig. 9(a)), and the liquid, gas, water, and heat flow (Fig. 9(b)) profiles calculated for three rather large values of intrinsic permeability, $k = 10^{-12}$, 10^{-13} , and 10^{-14} m², using the Verma *et al.* [19] relative permeability functions (Table 4) and the other values from Table 1. The most striking feature of Fig. 9(a) is the large decrease in heat-pipe length with decreasing permeability. Additionally, both heat-pipe temperature and temperature gradient increase with decreasing permeability, because a

larger pressure gradient is needed to drive fluid flow, and temperature depends on pressure through $T_{sat}(P_p)$. Conduction increases in the heat-pipe region as it becomes less isothermal. Figure 10 shows the same profiles for lower values of intrinsic permeability, $k = 10^{-15}$ and 10^{-17} m², again using the Verma relative permeability functions and the other values from Table 1. In the heat-pipe region, conduction becomes increasingly important relative to convection as permeability decreases, until for $k = 10^{-17}$ m² there is virtually no heat-pipe effect seen in Fig. 10(a). Because the saturation profile is quite sharp, the temperature profile for this case is very similar to the conduction-only profiles shown in Fig. 2; the liquid T profile is followed while $S_l > 0$, and a transition is made to the gas T profile at $S_l = 0$. In Figs. 9(b) and 10(b), the Q_g and Q_l profiles illustrate the decrease in heat-pipe counterflow for decreasing permeability. When permeability is large (Fig. 9(b), $k = 10^{-12}$ and 10^{-13} m²), the counterflow is large enough to transfer all heat convectively, and an extended region of constant Q_g and Q_l develops, corresponding to the isothermal zone seen in Fig. 9(a). For $k = 10^{-14}$ m², this region disappears. For smaller

Table 4. Relative permeability functions shown in Fig. 8(a)

| Function | k_{rl} | k_{rg} |
|--------------------------|---|---|
| Linear | S_1^* | $1 - S_1^*$ |
| Verma <i>et al.</i> [19] | S_1^{*3} | $1.259 - 1.7615S_1^{*2} + 0.5089S_1^{*2}$ |
| Cubic [12, 13] | S_1^{*3} | $(1 - S_1^*)^3$ |
| Corey [18] | S_1^{*4} | $(1 - S_1^*)^2(1 - S_1^{*2})$ |
| van Genuchten [20] | $(S_1^*)^{1/2}[1 - (1 - S_1^{*1/\lambda})^\lambda]^2, \lambda = 0.45$ | $1 - k_{rl}$ |

Note: S_1^* is reduced liquid saturation, defined in terms of irreducible liquid and gas saturations in various ways for the different relative permeability functions. For the present work, we assume all irreducible saturations to be zero, that is, neither liquid nor gas phase is ever immobile under two-phase conditions, so $S_1^* = S_1$.

values of permeability (Fig. 10(b)), there is no region of constant Q_g and Q_l , and the peak flow decreases in magnitude and shifts to more negative values of z . Despite the very different fluid flow patterns seen in Figs. 9(b) and 10(b), the heat-flow profile remains unchanged.

6.3. Heat-source strength

Figure 11 shows temperature and pressure (Fig. 11(a)), liquid-, gas-, and water-flow (Fig. 11(b)), and heat-flow (Fig. 11(c)) profiles calculated for heat-

source strength values of $Q_{e0} = 100, 200, 500,$ and 1000 W m^{-1} using the Verma relative permeability functions and the other values from Table 1. Figure 11(a) shows that larger values of Q_{e0} yield a shorter heat pipe and steeper conduction gradients, which shift the heat pipe to larger values of z . The overall pressure increase does not change very much with variations in Q_{e0} , so the heat-pipe temperature remains nearly constant.

Figures 11(b) and (c) show that the magnitude of the liquid-vapor counterflow is directly proportional

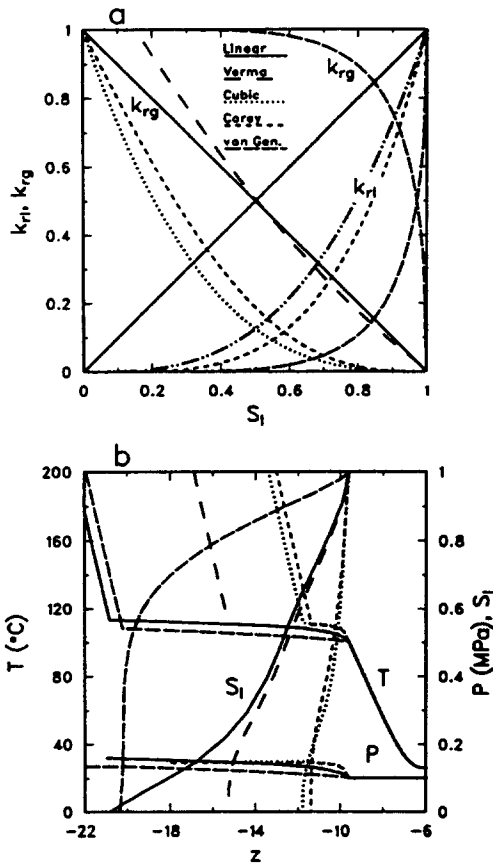


FIG. 8. Various relative permeability functions (a) and the temperature, pressure, and saturation profiles calculated using them (b). The relative permeability functions are described in Table 4.

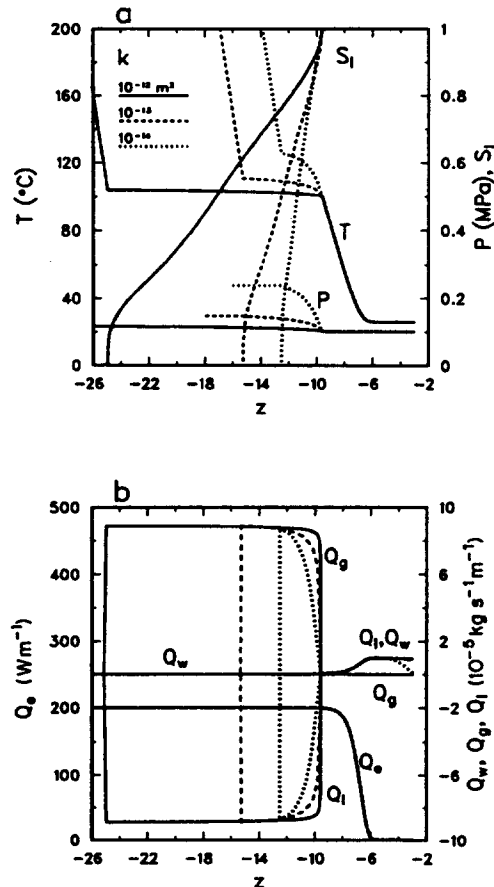


FIG. 9. Temperature, pressure, and saturation profiles (a) and heat-, mass-, liquid-, and gas-flow profiles (b) for several intrinsic permeability values.

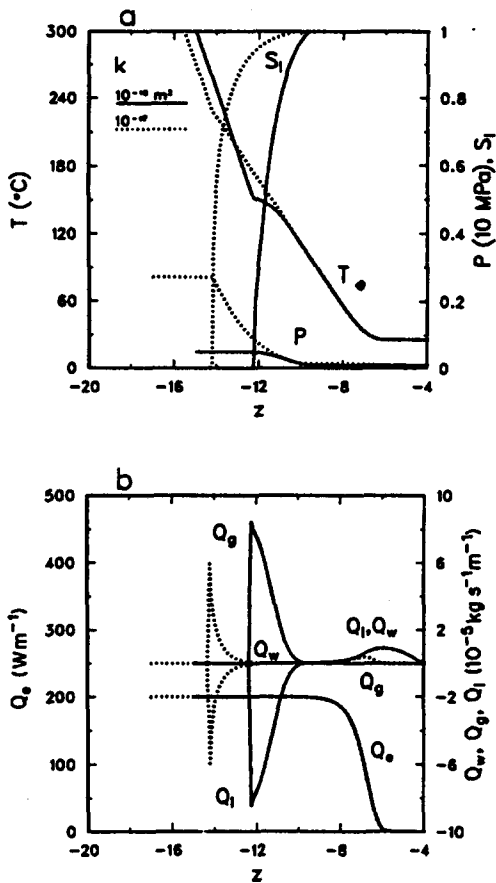


FIG. 10. Temperature, pressure, and saturation profiles (a) and heat-, mass-, liquid-, and gas-flow profiles (b) for low intrinsic permeability values.

to Q_e , demonstrating that heat transfer is convection dominated. In the liquid region beyond the heat pipe, liquid flow away from the heat source increases in magnitude with increasing Q_{e0} . Recall from the definition of z that a shift in heat-pipe location to larger values of z represents a heat pipe moving away from the heat source more rapidly. This rapid movement indicates more vapor formation, and requires a larger flow of liquid away from the heat source.

For low values of Q_{e0} (100 and 200 W m^{-1}), the heat-pipe region (with liquid flow toward the heat source) and outer liquid-flow region (with liquid flow away from the heat source) are well separated. However, as Q_{e0} increases and the conduction gradients become steeper, these two zones begin to overlap, resulting in a net decrease in the magnitude of liquid flow. Because vapor flow does not similarly decrease, a non-zero water flow (liquid plus vapor) develops in the heat-pipe region and a corresponding increase in heat flow occurs, as shown in Fig. 11(c). Further, for $Q_{e0} = 1000 \text{ W m}^{-1}$, the heat pipe occurs at such large values of z that the Q_e profile has already begun to decrease when the heat pipe begins, leading to an oscillation in Q_e .

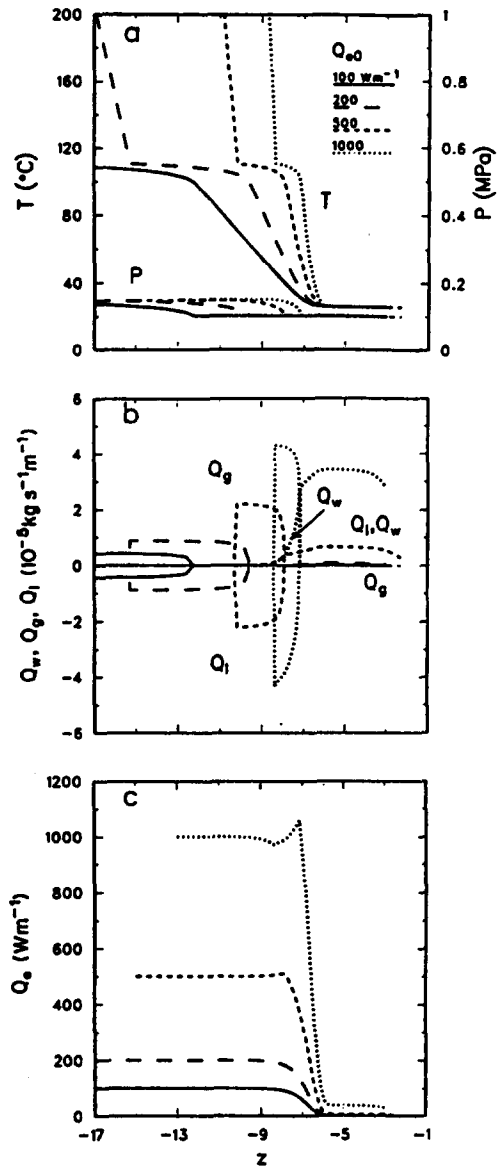


FIG. 11. The effect of heat-source strength on (a) temperature and pressure profiles, (b) mass-, liquid-, and gas-flow profiles, and (c) heat-flow profile.

6.4. Capillary pressure function

As is the case with relative permeability functions, a variety of capillary pressure functions have been used to describe fluid flow through porous media. Unlike relative permeabilities, which always vary between zero and one, the magnitude of the capillary pressure depends on other physical properties of the system, and this dependence makes it difficult to isolate the influence of capillary pressure function. Equation (48) shows that the saturation-profile slope is inversely proportional to $\partial P_c / \partial S_g$. However, we have seen that this slope is controlled by the liquid relative permeability function when S_l is small. Hence, capillary pressure functions that vary over the entire range

Table 5. Values of t_{sat} , the earliest time at which $T = T_{sat}$, for various initial conditions, calculated from equation (44) ($Q_{e0} = 500 \text{ W m}^{-1}$, $\kappa_c = 2.2 \text{ W m}^{-1} \text{ K}^{-1}$, $C_c = 2.4 \text{ MJ m}^{-3} \text{ K}^{-1}$, $r = 0.25 \text{ m}$)

| | Depth (m) | P_0 † (MPa) | T_0 ‡ (°C) | $T_{sat}(P_0)$ (°C) | t_{sat} (years) |
|---------------------|-----------|---------------|--------------|---------------------|-------------------|
| Partially saturated | 100 | 0.1 | 13 | 100 | 0.12 |
| | 300 | 0.1 | 19 | 100 | 0.08 |
| | 600 | 0.1 | 28 | 100 | 0.05 |
| Fully saturated | 300 | 3 | 19 | 234 | 137 |
| | 600 | 6 | 28 | 276 | 846 |
| | 900 | 9 | 37 | 303 | 2392 |
| | 1200 | 12 | 46 | 325 | 4722 |

† Atmospheric pressure for partially saturated cases, hydrostatic for fully saturated cases.

‡ $\nabla T = 30^\circ\text{C km}^{-1}$ with $T = 10^\circ\text{C}$ at zero depth.

of S_i , rather than primarily near S_{ir} , tend to produce longer heat pipes.

6.5. Rock compressibility

The value of rock compressibility, $\beta_r = 10^{-7} \text{ Pa}^{-1}$, used in the above examples is an order of magnitude greater than typical values found in nature. Using a more realistic value of $\beta_r = 10^{-8} \text{ Pa}^{-1}$, a calculation for the problem described in Table 1 yields identical results to those shown in Fig. 4, except that the outer liquid flow extends to larger values of z . As noted previously, small integration steps are necessary for large values of z , so extending the limits of integration to large z requires increased computational effort. As long as the rock compressibility used is small relative to gas-phase and two-phase water compressibilities, it will affect only the solution in the liquid zone.

6.6. Initial conditions

Initial temperature T_0 and pressure P_0 greatly influence the fluid and heat flows that occur in response to a heat source. For a heat pipe to develop, the fluid must be volatile, that is, near its saturation temperature, which is determined by P_0 . For partially

saturated media, T_0 increases with depth while P_0 and, therefore, $T_{sat}(P_0)$ remain essentially constant. Thus, the temperature around a deep heat source increases from T_0 to T_{sat} in a shorter length of time (larger value of η) than does the temperature around a shallow heat source. For fully saturated media, both T_0 and P_0 increase as depth increases, with $T_{sat}(P_0)$ growing more rapidly than T_0 . Thus, $T = T_{sat}$ at a later time (smaller value of η) for a deeper heat source. Equation (44) for the conduction-only temperature distribution may be used to determine η_{sat} , the largest value of η for which $T \geq T_{sat}$. For a given radial distance, η_{sat} determines the earliest time after waste emplacement when saturation temperature is reached; this time is denoted t_{sat} . Table 5 shows t_{sat} for various heat-source depths, calculated using equation (44) and a value of $r = 0.25 \text{ m}$. It is apparent that P_0 plays the dominant role in controlling t_{sat} . If we allow for the heat-source strength decline with time that is characteristic of nuclear waste repositories, it is unlikely that saturation temperature will ever be reached for the fully saturated cases in Table 5.

Table 6 shows t_{sat} for some proposed repository conditions. As expected, t_{sat} is smallest for the partially saturated Yucca Mountain site. Despite the large value of P_0 , the value of t_{sat} is also quite small for the Stripa site because of the high heat-flow rate $Q_{e0} = 1385 \text{ W m}^{-1}$. Similarly, the large value of t_{sat} for the Mol-Dessel site is largely due to the low heat-flow rate $Q_{e0} = 300 \text{ W m}^{-1}$.

The P_0 values in Table 6 are based on an initial repository pressure that is equal to the ambient pressure. For repositories in fully saturated media, this is not a good assumption if the repository is ventilated with atmospheric air or if backfill pressure is less than ambient pressure. In this case, non-uniform initial conditions preclude use of the similarity transformation and the results presented in this paper are not applicable. Although two-phase conditions may evolve, heat-pipe development is not expected under these circumstances, because a driving force for gas-phase flow away from the heat source is required for

Table 6. Values of t_{sat} , the earliest time at which $T = T_{sat}$, for various proposed repository sites, calculated from equation (44) with $r = 0.25 \text{ m}$. The granite, basalt, and clay sites are water saturated

| Geologic setting (example site) | Repository depth (m) | P_0 (MPa) | T_0 (°C) | T_{sat} (°C) | κ_c ($\text{W m}^{-1} \text{ K}^{-1}$) | C_c ($\text{MJ m}^{-3} \text{ K}^{-1}$) | Age of waste (years) | Q_{e0} (W m^{-1}) | t_{sat} (years) |
|--|----------------------|-------------|------------|----------------|---|---|----------------------|--------------------------------|-------------------|
| Partially saturated tuff [21] (Yucca Mountain, U.S.A.) | 348 | 0.1 | 24 | 100 | 2.3 | 2.4 | 8 | 636† | 0.03 |
| Granite [22, 23] (Stripa, Sweden) | 340 | 2 | 10 | 212 | 3.2 | 2.1 | 5 | 1385 | 0.21 |
| Basalt [24] (Hanford, U.S.A.) | 900 | 9 | 33 | 303 | 2.3 | 2.7 | 10 | 691 | 85 |
| Clay [25] (Mol-Dessel, Belgium) | 220 | 2.2 | 16 | 217 | 1.7 | 2.8 | 50 | 300† | 2456 |

† Not given in reference, estimated from information on areal loading, age of waste, and emplacement configuration.

a heat pipe to occur. This force is absent if the pressure at the heat source is less than the ambient pressure.

7. SUMMARY AND CONCLUSIONS

The mass and energy transport equations for one-dimensional radial flow in a homogeneous porous medium depend on time t and distance r only through the similarity variable $\eta = r/\sqrt{t}$. If initial and boundary conditions can be written as functions of η , then the entire flow problem can be solved in terms of the similarity variable. A practically important case for which this is possible is that involving a constant-rate line source at $r = 0$ and uniform initial conditions.

We have applied the similarity variable concept to solve an idealized version of the problem of fluid and heat flow near high-level nuclear waste packages emplaced in geologic media. The cylindrical waste package is approximated by a linear heat source at $r = 0$. By means of the similarity transformation, the partial differential equations for fluid and heat flow are converted to a set of ordinary differential equations in η . These ordinary differential equations can be solved with the iterative 'shooting method'. The accuracy and efficiency of the similarity solution approach has been demonstrated by comparison with numerical finite-difference simulations. We have presented illustrative examples to show the dependence of fluid- and heat-flow patterns and heat-pipe conditions on relative and absolute permeability and on other parameters of interest.

The most important application of the approach developed in this paper is for the evaluation of thermohydrologic conditions that will develop near high-level nuclear waste packages emplaced in the partially saturated fractured tuffs at Yucca Mountain. A realistic appraisal will require solving the full equation system, including air, and making provisions for dealing with the extremely non-linear relative permeability relationships characteristic of a fractured-porous medium [8]. This approach appears quite feasible and is currently under development. A peculiar issue in nuclear waste disposal arises from the decline of heat output with time. However, the constant-rate solution obtainable from the similarity method will give an acceptable approximation for the early time period (tens of years) when thermal effects in the host rock are strongest. Long-time predictions for a heat source with strength maintained constant at the initial rate are also useful because they provide conservative limits for thermohydrologic effects. The similarity solution can also serve as a benchmark for testing the accuracy of complex numerical simulators for multiphase fluid and heat flow.

Acknowledgements—The careful review of this work by Y. W. Tsang and R. W. Zimmerman of Lawrence Berkeley Laboratory, M. E. Fewell and M. Martinez of Sandia National Laboratories, and two anonymous reviewers is gratefully appreciated. This work was supported, in part, by the Nuclear Waste Repository Technology Department,

Sandia National Laboratories, and the Director, Office of Energy Research, Office of Basic Energy Sciences, Division of Engineering and Geosciences, of the U.S. Department of Energy under Contract No. DE-AC03-76SF00098.

REFERENCES

1. K. Pruess, Y. W. Tsang and J. S. Y. Wang, Modeling of strongly heat driven flow in partially saturated fractured porous media. In *Memoirs, International Association of Hydrogeologists*, Vol. XVII, pp. 486–497 (1985).
2. C. Doughty and K. Pruess, A semianalytical solution for heat pipe effects near high-level nuclear waste packages buried in partially saturated geological media, *Int. J. Heat Mass Transfer* 31, 79–90 (1988).
3. M. J. O'Sullivan, A similarity method for geothermal well test analysis, *Water Resour. Res.* 17(2), 390–398 (1981).
4. M. A. Grant, Quasi-analytic solutions for two-phase flow near a discharging well, Report 86, Applied Mathematics Division, Department of Scientific and Industrial Research, Wellington, New Zealand (1979).
5. Y. W. Tsang and C. F. Tsang, An analytic study of geothermal reservoir pressure response to cold water reinjection, *Proc. Fourth Annual Workshop on Geothermal Reservoir Engng*, SGP-TR-30, pp. 322–331. Stanford University, Stanford, California (1978).
6. G. de Marsily, *Quantitative Hydrogeology*, p. 74. Academic Press, Orlando, Florida (1986).
7. W. H. Press, B. P. Flannery, S. A. Teukolsky and W. T. Vetterling, *Numerical Recipes: The Art of Scientific Computing*, Chap. 16. Cambridge University Press, New Rochelle, New York (1986).
8. K. Pruess, J. S. Y. Wang and Y. W. Tsang, On thermohydrological conditions near high-level nuclear wastes emplaced in partially saturated fractured tuff. Part 2: effective continuum approximation, *Water Resour. Res.* (1990), in press.
9. K. S. Udell and J. S. Fitch, Heat and mass transfer in capillary porous media considering evaporation, condensation, and non-condensable gas effects, *Proc. 23rd ASME/AIChE National Heat Transfer Conf.*, HTD Vol. 46, *Heat Transfer in Porous Media and Particulate Flows*. American Society of Mechanical Engineers (1985).
10. W. H. Somerton, J. A. Keese and S. L. Chu, Thermal behavior of unconsolidated oil sands, Paper SPE-4506, 48th Annual Fall Meeting of the Society of Petroleum Engineers, Las Vegas, Nevada (1973).
11. W. H. Somerton, A. H. El-Shaarani and S. M. Mobarak, High temperature behavior of rocks associated with geothermal type reservoirs, Paper SPE-4897, 44th Annual California Regional Meeting of the Society of Petroleum Engineers, San Francisco, California (1974).
12. I. Fatt and W. A. Klikoff, Effect of fractional wettability on multiphase flow through porous media, AIME Technical Note No. 2043, *AIME Trans.* 216, 246 (1959).
13. M. R. J. Wyllie, Relative permeability. In *Petroleum Production Handbook* (Edited by T. C. Frick), Vol. 2, Chap. 25. McGraw-Hill, New York (1962).
14. M. C. Leverett, Capillary behavior in porous solids, *AIME Trans.* 142, 152–169 (1941).
15. H. S. Carslaw and J. C. Jaeger, *Conduction of Heat in Solids* (2nd Edn), pp. 261–262. Oxford University Press, Oxford (1959).
16. K. Pruess, TOUGH user's guide, Report NUREG/CR-4645, Nuclear Regulatory Commission, Washington, DC (1987).
17. R. C. Schroeder, M. J. O'Sullivan, K. Pruess, R. Celati and C. Ruffilli, Reinjection studies of vapor-dominated systems, *Geothermics* 11(2), 93–119 (1982).
18. A. T. Corey, The interrelation between gas and oil relative permeabilities, *Producers Monthly* Nov., 38–41 (1954).

19. A. K. Verma, K. Pruess, C. F. Tsang and P. A. Witherspoon, A study of two-phase concurrent flow of steam and water in an unconsolidated porous medium. *Proc. 23rd ASME/AIChE National Heat Transfer Conf.*, HTD Vol. 46, *Heat Transfer in Porous Media and Particulate Flows*, pp. 135–143. American Society of Mechanical Engineers (1985).
20. M. Th. van Genuchten, A closed-form equation for predicting the hydraulic conductivity of unsaturated soils. *Soil Sci. Soc. Am. J.* **44**, 892–898 (1980).
21. Y. W. Tsang and K. Pruess, A study of thermally induced convection near a high-level nuclear waste repository in partially saturated fractured tuff. *Water Resour. Res.* **23**(10), 1958–1966 (1987).
22. P. A. Witherspoon, N. G. W. Cook and J. E. Gale, Progress with field investigations at Stripa, Report LBL-10559 (SAC-27), Lawrence Berkeley Laboratory, Berkeley, California (1980).
23. I. Javandel and P. A. Witherspoon, Thermal analysis of the Stripa heater test data from the full scale drift. Report LBL-13217 (SAC-43), Lawrence Berkeley Laboratory, Berkeley, California (1981).
24. A. Verma and K. Pruess, Thermohydrological conditions and silica redistribution near high-level nuclear wastes emplaced in saturated geological formations. *J. Geophys. Res.* **93**(B2), 1159–1173 (1988).
25. L. H. Baetlslé, A. Bonne, P. Henrion, M. Put and J. Patyn, Assessment of the combined effects of temperature increase, water convection, migration of radionuclides, and radiolysis on the safety of a nuclear waste repository in the boom clay. In *Coupled Processes Associated with Nuclear Waste Repositories* (Edited by C. F. Tsang), pp. 225–236. Academic Press, Orlando, Florida (1987).
26. International Formulation Committee, *A Formulation*

of the Thermodynamic Properties of Ordinary Water Substance. IFC Secretariat, Düsseldorf, Germany (1967).

APPENDIX: THERMOPHYSICAL PROPERTIES

The constitutive relationships used to define the thermodynamic parameters in terms of the primary variables are taken from the numerical model TOUGH [16], described in Section 5.

Steam tables, given by the International Formulation Committee [26], provide closed-form expressions for ρ , u , h , μ , and σ (used in P_c) as functions of P and T . Saturation temperature T_{sat} is considered to be solely a function of gas-phase pressure P_g ; that is, vapor-pressure lowering is neglected.

Relative permeabilities k_{rl} and k_{rg} and capillary pressure P_c are functions of liquid and gas saturation S_l and S_g ; examples are shown in Tables 1 and 4. Thermal conductivity κ also varies with liquid saturation, as given by [10, 11]

$$\kappa = \kappa_g + (S_l)^{1/2}(\kappa_l - \kappa_g) \quad (\text{A1})$$

where κ_g and κ_l are the values of thermal conductivity for dry and liquid-saturated rock, respectively.

Porosity depends on pressure and temperature

$$\phi = \phi_0 \exp [\beta_r(P - P_0) + \alpha_r(T - T_0)] \quad (\text{A2})$$

where β_r and α_r are constant rock compressibility and rock expansivity, respectively, and ϕ_0 is the value of porosity for $P_g = P_0$ and $T = T_0$.

Intrinsic permeability k , rock density ρ_r , and rock specific heat c_r are assumed to be constants. The relationships needed for two-component systems including air are not included here, but may be found in the description of TOUGH [16].

SOLUTION DE SIMILITUDE POUR UN FLUIDE DIPHASIQUE ET LE FLUX DE CHALEUR PRES DE DECHETS FORTEMENT RADIOACTIFS PLACES DANS DES MILIEUX POREUX

Résumé—L'emplacement d'une source de chaleur telle qu'un lot de déchets fortement nucléaire, dans un milieu géologique provoque un couplage intense entre les comportements thermiques et hydrologiques. Dans certaines conditions, un caloduc se développe avec un impact significatif sur les conditions à la source de chaleur. Dans un milieu infini, homogène et perméable avec une source thermique linéaire uniforme, les équations aux dérivées partielles pour une géométrie radiale peuvent être transformées en équations différentielles en utilisant une variable de similitude $\eta = r/\sqrt{t}$. Ces équations sont intégrées numériquement en utilisant une méthode de tir itérative pour avoir une description des températures, des pressions, de la saturation, du flux thermique, du débit masse de gaz et de liquide autour de la source. La solution est vérifiée par des simulations numériques aux différences finies. Des solutions sont données pour un domaine de paramètres hydrologiques et thermiques et on discute le comportement de caloduc pour certaines conditions.

EINE ÄHNLICHKEITSLÖSUNG FÜR ZWEIFHASEN-STRÖMUNG UND WÄRMEÜBERGANG IN DER UMGEBUNG VON, IN EINEM PORÖSEN MEDIUM EINGELAGERTEM, HOCH-RADIOAKTIVEM ATOMMÜLL

Zusammenfassung—Die Einbettung einer Wärmequelle, z. B. die Einlagerung von hoch-radioaktivem Atommüll, in ein geologisches Umfeld, führt zu stark gekoppelten thermischen und hydrologischen Vorgängen. Unter gewissen Umständen kann sich eine Art Wärmerohr entwickeln, welches erhebliche Auswirkungen auf die Zustände an der Wärmequelle besitzt. In einem unendlichen, homogenen und durchlässigen Medium mit einer linearen Wärmequelle konstanter Leistung können die partiellen Differentialgleichungen für das umgebende Fluid zur Bestimmung der radialen Wärmeströme angegeben werden. Diese Gleichungen können durch das Einführen einer Ähnlichkeitsvariablen der Form $\eta = r/\sqrt{t}$ in gewöhnliche Differentialgleichungen umgewandelt werden. Werden diese Gleichungen mit einer 'shooting'-Methode auf numerischem Wege integriert, so können die Temperatur-, Druck- und Sättigungsbedingungen sowie die Wärme-, Gas- und Flüssigkeitsströmungen in der Umgebung der Wärmequelle angegeben werden. Die Ähnlichkeitslösung wird mit Hilfe einer numerischen Finite-Differenzen-Methode überprüft. Grafische Darstellungen der Lösungen werden für eine Reihe von hydrologischen und thermischen Parametern angegeben. Abschließend wird die Wahrscheinlichkeit der Entstehung eines Wärmerohrs für die Bedingungen an verschiedenen vorgeschlagenen Lagerstätten diskutiert.

АВТОМОДЕЛЬНОЕ РЕШЕНИЕ ДЛЯ ПОТОКА ДВУХФАЗНОЙ ЖИДКОСТИ И ТЕПЛА У
КОНТЕЙНЕРОВ С ЯДЕРНЫМИ ОТХОДАМИ С ВЫСОКИМ УРОВНЕМ РАДИАЦИИ,
ПОМЕЩЕННЫХ В ПОРИСТЫЕ СРЕДЫ

Аннотация—Источник тепла (контейнер с радиоактивными отходами), помещенный в геологическую среду, вызывает сильные изменения в ее тепловом и гидрологическом поведении. При определенных условиях среду можно рассматривать как тепловую трубу, оказывающую воздействие на условия у источника тепла. В случае бесконечной однородной проницаемой среды с линейным источником тепла постоянной мощности можно преобразовать дифференциальные уравнения в частных производных, определяющие потоки жидкости и тепла в радиальной геометрии, в обыкновенные дифференциальные уравнения с использованием переменной подобия $\eta = r/\sqrt{t}$. Данные уравнения численно интегрируются итерационным методом “пристрелки” с целью описания полей температуры, давления, насыщения, теплового потока, а также потоков газа и жидкости вокруг такого источника тепла. Автомоделное решение подтверждается с помощью численных методов конечных разностей. Приводятся иллюстративные решения для ряда гидрологических и тепловых параметров. Обсуждается вероятность образования тепловой трубы в условиях нескольких предложенных расположений хранилищ ядерных отходов.